AIAA JOURNAL
Vol. 41, No. 10, October 2003

Thermoelastic Modeling and Vibration of Functionally Graded Thin-Walled Rotating Blades

Sang-Yong Oh* and Liviu Librescu†
Virginia Polytechnic Institute and State University, Blacksburg, Virginia 24061
and
Ohseop Song‡
Chungnam National University, Daejon City 305-764, Republic of Korea

Thermoelastic modeling and vibration of turbomachinery thin-walled rotating blades made of functionally graded ceramic-metal based materials are studied. In this context, the case of pretwisted and tapered thin-walled beams, rotating with a constant angular velocity and exposed to a steady temperature field of a prescribed gradient through the blade wall thickness, is considered. The study is achieved by varying the volume fraction of the ceramic and metallic constituents with the help of a simple power law distribution and by accounting for the temperature-dependent material properties. The governing dynamic equations that are established are expressed in terms of one-dimensional displacement measures. Because of their general character, static and dynamic problems involving rotating blades operating in the conditions of a high-temperature environment can be solved. The numerical results highlight the effects of the volume fraction, temperature gradient, taper ratio, and pretwist on the bending–bending coupled/uncoupled free-vibration characteristics, and pertinent conclusions are outlined.

Introduction

FUNCTIONALLY graded materials (FGMs) for high-temperature structural applications are special composites, microscopically inhomogeneous, whose thermomechanical properties vary smoothly and continuously in predetermined directions throughout the body of the structure. This feature is achieved by gradually varying the volume fraction of constituent materials, which usually are from ceramics and metals.

The ceramic in a FGM offers thermal barrier effects and protects the metal from corrosion and oxidation, whereas the FGM is toughened and strengthened by the metallic composition. As a result, these materials are able to withstand high-temperature gradients, without structural failure.

In contrast to standard laminated composite structures, whose material properties are piecewise constant through their thickness and, as a result, are exposed to adverse interface effects that can yield the failure of the structure, in the case of the FGMs due to the continuous variation of their material properties, such effects do not occur.

In addition to the research work devoted to modeling of three-dimensional FGM media, for example, Refs. 1 and 2, the studies involving thin-walled structures made of FGMs have been mainly devoted to beams, plates, and shells.[3–16] To the best of the authors' knowledge, in spite of its evident practical importance, no research work related to the modeling and behavior of rotating blades operating in a high-temperature environment and made of FGMs has been yet accomplished. This paper is devoted to this topic.

Herein, the case of a straight, pretwisted tapered thin-walled beam rotating with a constant angular velocity and exposed to a steady temperature field experiencing a gradient through the blade thickness is considered. It is assumed that the blade is made of FGMs whose properties vary continuously across the blade thickness and that the material properties are temperature dependent. In this context, both the modeling and the vibrational behavior of rotating blades are investigated, and pertinent conclusions are outlined.

This paper represents an extension for this case of a number of results previously obtained.[17–21] The obtained results highlight the great performances obtained when the FGM concept is applied in this context.

Structural Model: Basic Assumptions

The case of a straight, tapered, and pretwisted flexible beams of length L, rotating with the constant angular velocity Ω normal to the plane of rotation is considered. The origin of the rotating axis system (x, y, z) is located at the blade root at an offset R_0 from the rotation axis (Fig. 1). Whereas z is the spanwise coordinate, x and y are the cross-section coordinates (Fig. 1). Besides the coordinates (x, y, z), the coordinates (x^p, y^p, z^p) are also considered, where x^p and y^p are the principles axes of an arbitrary beam cross section. The two coordinate systems are related by the following transformation formula[19,20]:

$$x(s, z) = x^p(s)\cos\beta(z) - y^p(s)\sin\beta(z) \tag{1a}$$

$$y(s, z) = x^p(s)\sin\beta(z) + y^p(s)\cos\beta(z) \tag{1b}$$

$$z = z^p \tag{1c}$$

where s is the circumferential coordinate, $\beta(z) = \beta_0 z/L$ is the pretwist of the current section, β_0 is the pretwist at the beam tip, and L is the beam span.

In addition, the local coordinate system (s, z, n) is also adopted, where s and n are the circumferential and thickness wise coordinates, respectively, and $|n| \le h/2$, where h is the wall blade thickness.

It is assumed that the beam is tapered in both the chordwise and height directions. As a result, the variation along the blade span of the chord $c(z)$ and height $b(z)$ of the midline cross-sectional profiles are expressed as

$$c(z) = [1 + (z/L)(\alpha_c - 1)]c_R, \qquad b(z) = [1 + (z/L)(\alpha_h - 1)]b_R \tag{2}$$

where $\alpha_c = c_T/c_R$ and $\alpha_h = b_T/b_R$ define the taper ratios of the chord and height, respectively, where T and R identify the blade characteristics at the tip and root cross sections, respectively. For further use, we define the parameter $S(z) \equiv b(z)/c(z)$. It is clear that, when $\alpha_h = \alpha_c$, then $S(z) \Rightarrow S = b_R/c_R$.

Received 13 August 2002; revision received 15 February 2003; accepted for publication 25 March 2003.

*Research Associate, Department of Engineering Science and Mechanics.
†Professor, Department of Engineering Science and Mechanics.
‡Professor, Mechanical Engineering Department.

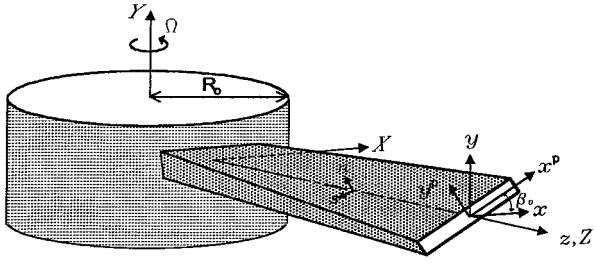

Fig. 1a Configuration of tapered pretwisted turbine blades.

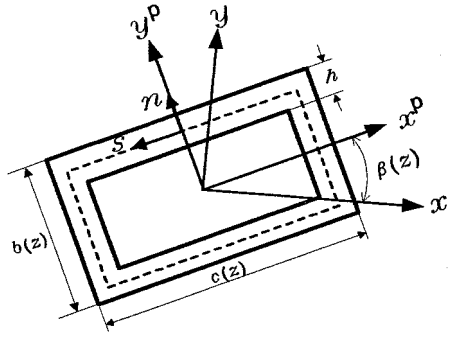

Fig. 1b Blade cross section.

From Eqs. (2) it becomes apparent that for $(\alpha_c, \alpha_h) < 1$ there is a decay of the chord and height toward the blade tip, whereas when $(\alpha_c, \alpha_h) > 1$, the opposite trend occurs, that is, the decay is toward the blade root.

Besides the defined coordinate systems, the inertial reference systems (X, Y, Z) is attached to the center of the hub O (Fig. 1). We define the unit vectors associated with the frame coordinates (x, y, z) and (X, Y, Z), by $(\boldsymbol{i}, \boldsymbol{j}, \boldsymbol{k})$ and $(\boldsymbol{I}, \boldsymbol{J}, \boldsymbol{K})$, respectively.

Within the present work, the precone and stagger of the blade are assumed to be zero. It is further assumed that the rotation takes place in the plane (X, Z) with the constant angular velocity $\boldsymbol{\Omega}$, with the spin axis along the Y axis. The beam spanwise z-coordinate axis coincides with a straight unspecified reference axis.

For the modeling of the FGM rotating blade, a number of assumptions are adopted: 1) The case of a single-cell, thin-walled beam is considered. 2) The original cross section of the blade is preserved. 3) Transverse shear, rotatory inertia, and centrifugal accelerations are included.

Kinematics

As in previous work,[17–21] the components of the three-dimensional displacement vector are expressed as

$$u(x, y, z; t) = u_0(z; t) - y\phi(z; t)$$

$$v(x, y, z; t) = v_0(z; t) + x\phi(z; t)$$

$$w(x, y, z; t) = w_0(z; t) + \theta_x(z; t)\left[y(s) - n\frac{\mathrm{d}x}{\mathrm{d}s}\right]$$

$$+\theta_y(z; t)\left[x(s) + n\frac{\mathrm{d}y}{\mathrm{d}s}\right] - \phi'(z; t)[F_w(s) + na(s)] \tag{3}$$

where $u_0(z; t)$, $v_0(z; t)$, and $w_0(z; t)$ are the rigid-body translations along the x, y, and z axes, $\theta_x(z; t), \theta_y(z; t)$, and $\phi'(z; t)$ are the rigid-body rotations about the x and y axes and the twist about the z axis. The expressions for $\theta_x(z; t)$ and $\theta_y(z; t)$ are

$$\theta_x(z; t) = \gamma_{yz}(z; t) - v_0'(z; t), \qquad \theta_y(z; t) = \gamma_{xz}(z; t) - u_0'(z; t) \tag{4}$$

In Eq. (3c), $F_w(s)$ and $na(s)$ play the role of primary and secondary warping functions, respectively, and γ_{yz} and γ_{xz} denote the transverse shear strains. For nonshearable blades, $\theta_x(z, t) = -v_0'(z, t)$ and $\theta_y(z, t) = -u_0'(z, t)$.

The position vector of a point $M(x, y, z)$ belonging to the deformed structure is

$$\boldsymbol{R}(x, y, z; t) = (x + u)\boldsymbol{i} + (y + v)\boldsymbol{j} + (z + w)\boldsymbol{k} + \boldsymbol{R}_0 \tag{5}$$

Recalling that the spin rate was assumed to be constant, keeping in mind that the rotation takes place solely in the XZ plane, and making use of equations expressing the time derivatives of unit vectors $(\boldsymbol{i}, \boldsymbol{j}, \boldsymbol{k})$, one obtains the velocity and acceleration vectors of an arbitrary point M of the beam in the form

$$\dot{\boldsymbol{R}} = V_x\boldsymbol{i} + V_y\boldsymbol{j} + V_z\boldsymbol{k} \tag{6a}$$

$$\ddot{\boldsymbol{R}} = a_x\boldsymbol{i} + a_y\boldsymbol{j} + a_z\boldsymbol{k} \tag{6b}$$

Their components are

$$V_x = \dot{u} + (R_0 + z + w)\Omega \tag{7a}$$

$$V_y = \dot{v} \tag{7b}$$

$$V_x = \dot{w} - (x + u)\Omega \tag{7c}$$

$$a_x = \ddot{u} + \underline{2\dot{w}\Omega} - \underline{\underline{(x + u)\Omega^2}} \tag{7d}$$

$$a_y = \ddot{v} \tag{7e}$$

$$a_z = \ddot{w} - \underline{2\dot{u}\Omega} - \underline{\underline{(R_0 + z + w)\Omega^2}} \tag{7f}$$

In these equations and the following ones, the superposed dots denote time derivatives, whereas the terms underscored by one and two solid lines are associated with Coriolis and centrifugal inertia terms, respectively.

In the forthcoming development, the study will be restricted to the case involving the coupling between transversal bending (flapping), lateral bending (lagging), and transverse shear. Such coupling occurs only for pretwisted blades. In the absence of pretwist, as it will be seen, the flapping and lagging motion become decoupled. The twist appears to be decoupled from the bending–bending motion. By virtue of displacement representations, Eqs. (3), in the framework of purely bending motions, the strain measures assume the following form.

Axial strain:

$$\varepsilon_{zz}(n, s, z, t) = \bar{\varepsilon}_{zz}(s, z, t) + n\bar{\bar{\varepsilon}}_{zz}(s, z, t) \tag{8a}$$

where

$$\bar{\varepsilon}_{zz}(s, z, t) = \theta_x'(z, t)y(s, z) + \theta_y'(z, t)x(s, z) \tag{8b}$$

$$\bar{\bar{\varepsilon}}_{zz}(s, z, t) = \theta_y'(z, t)\frac{\mathrm{d}y}{\mathrm{d}s} - \theta_x'(z, t)\frac{\mathrm{d}x}{\mathrm{d}s} \tag{9}$$

are the axial strains associated with the primary and secondary warping, respectively.

Tangential shear strain:

$$\varepsilon_{sz}(n, s, z, t) \equiv \bar{\varepsilon}_{sz}(s, z, t) \tag{10a}$$

where

$$\bar{\varepsilon}_{sz}(s, z, t) = [\theta_y(z, t) + u_0'(z, t)]\frac{\mathrm{d}x}{\mathrm{d}s} + [\theta_x(z, t) + v_0'(z, t)]\frac{\mathrm{d}y}{\mathrm{d}s} \tag{10b}$$

Transverse shear strain:

$$\varepsilon_{nz}(s, z, t) = [\theta_y(z, t) + u_0'(z, t)]\frac{\mathrm{d}y}{\mathrm{d}s} - [\theta_x(z, t) + v_0'(z, t)]\frac{\mathrm{d}x}{\mathrm{d}s} \tag{11}$$

Three-Dimensional Constitutive Equations for Functionally Graded Blades

The design of advanced turbine blades must meet high efficiency and high reliability, regardless of the severe temperature gradients under which these may operate. To this end, functionally graded ceramic–metal-based materials are used.

Because these materials are isotropic, the corresponding thermoelastic constitutive law adapted to the case of thin-walled structures is expressed as

$$\begin{bmatrix} \sigma_{ss} \\ \sigma_{zz} \\ \sigma_{zn} \\ \sigma_{ns} \\ \sigma_{sz} \end{bmatrix} = \begin{bmatrix} Q_{11} & Q_{12} & 0 & 0 & 0 \\ Q_{12} & Q_{11} & 0 & 0 & 0 \\ 0 & 0 & Q_{44} & 0 & 0 \\ 0 & 0 & 0 & Q_{44} & 0 \\ 0 & 0 & 0 & 0 & Q_{66} \end{bmatrix} \begin{bmatrix} \varepsilon_{ss} \\ \varepsilon_{zz} \\ \varepsilon_{zn} \\ \varepsilon_{ns} \\ \varepsilon_{sz} \end{bmatrix} - \begin{bmatrix} \hat{\alpha}\Delta T \\ \hat{\alpha}\Delta T \\ 0 \\ 0 \\ 0 \end{bmatrix} \tag{12}$$

The reduced thermoelastic coefficients are defined as

$$Q_{11} = E/(1-\nu^2) \tag{13a}$$

$$Q_{12} = E\nu/(1-\nu^2) \tag{13b}$$

$$Q_{66} = E/2(1+\nu)(\equiv G) \tag{13c}$$

$$Q_{44} = Q_{55} = k^2 G \tag{13d}$$

$$\hat{\alpha} = E\alpha/(1-\nu) \tag{13e}$$

where E and ν are the Young's modulus and Poisson's ratio, respectively, k^2 is the transverse shear correction factor, $\Delta T(s,\ z,\ n)$ is the steady-state temperature rise from that of the stress-free state, and α is the thermal expansion coefficient. Although assumed to be large, the temperature rise cannot be so extreme as not to trigger elastoplastic or viscoelastic responses, for the metallic constituent.

For a model of ceramic–metal FGM, the material properties vary continuously across the blade thickness according to the law

$$E(n) = (E_c - E_m)V_m + E_m \tag{14a}$$

$$\nu(n) = (\nu_c - \nu_m)V_m + \nu_m \tag{14b}$$

$$V_c = 1 - V_m \tag{14c}$$

$$\rho(n) = (\rho_c - \rho_m)V_m + \rho_m \tag{14d}$$

$$\alpha(n) = (\alpha_c - \alpha_m)V_m + \alpha_m \tag{14e}$$

where V_m and V_c are the volume fractions of metal and ceramic components and subscripts m and c identify the quantities affiliated to metal and ceramic, respectively.

For the case of a uniform blade thickness and of a reference surface at $n=0$, V_m can be expressed as[6–11]

$$V_m = [(2n+h)/2h]^K \tag{15}$$

where $K, 0 \le K \le \infty$, is the volume fraction parameter. From Eqs. (14) considered in conjunction with Eq. (15), it results that for $n = h/2$, $E \to E_c$, $\nu \to \nu_c$, and $\rho \to \rho_c$, whereas for $n = -h/2$, $E \to E_m$, $\nu \to \nu_m$, and $\rho \to \rho_m$.

This shows that, consistent with this law, the material properties vary continously from the top surface of the blade, where the material is entirely ceramic, to fully metal at the bottom surface. From Eqs. (14) when started with $K=0$, for which the blade is entirely from ceramic, it also becomes evident that the increase of the volume fraction parameter K implies a continuous increase of the metal content to the detriment of the ceramic.

As a result, the compositional material profile of the FGM blade is governed by the specific value of the volume fraction parmeter K. As an example, consider the case when $K=1$. In such a case, $P(n) = (P_c + P_m)/2 + n(P_c - P_m)/h$, where P is one of the generic properties of the material. Again, for $n = h/2$ and $n = -h/2$, the blade properties belong to ceramic and metal, respectively.

It is also evident that on the blade middle surface, that is, when $n=0$,

$$P(0) = (P_c + P_m)/2 \tag{16}$$

whereas for $n > 0$ and $n < 0$, the blade material consisting of a mixture of both constituents tends to be ceramic and metal dominated, respectively.

It is assumed that the blade is subjected to a steady-state one-dimensional temperature distribution through its thickness.

The steady-state equation of the one-dimensional heat transfer is expressed by

$$\frac{\mathrm{d}}{\mathrm{d}n}\left[\kappa(n)\frac{\mathrm{d}T}{\mathrm{d}n}\right] = 0 \tag{17}$$

and the boundary conditions are $T(h/2) = T_t$ and $T(-h/2) = T_b$, where $\kappa(n)$ is the thermal conductivity in the thickness direction and T_t and T_b are the temperatures at the top and bottom surfaces of the FGM blade, respectively.

The solution of Eq. (17) in conjunction with the conditions on bounding surfaces yields the steady-state temperature distribution $T(n)$:

$$T(n) = T_b\left\{1 + \left[\lambda \Big/ \int_{-h/2}^{h/2} \frac{\mathrm{d}n}{\kappa(n)}\right] \int_{-h/2}^{n} \frac{\mathrm{d}n}{\kappa(n)}\right\} \tag{18a}$$

where

$$\lambda = (T_t - T_b)/T_b \tag{18b}$$

represents a measure of the normalized temperature gradient across the blade wall thickness. Throughout the numerical simulations, $T_b = 300$ K will be considered.

The thermal conductivity $\kappa(n)$ of the FGM is assumed to vary according to the law

$$\kappa(n) = (\kappa_c - \kappa_m)V_m + \kappa_m \tag{19}$$

and the thermal conductivities κ_c and κ_m are temperature independent.

In contrast to this assumption, the remaining properties of the FGM are temperature dependent and vary according to the law obtained from experiments. These are expressed in generic form as

$$P(n) = P_0\left(P_{-1}\big/T + 1 + P_1 T + P_2 T^2 + P_3 T^3\right) \tag{20}$$

where P_0, P_{-1}, P_1, P_2, and P_3 are the constants in the cubic fit of the specific temperature-dependent material property, where T (in Kelvin) is the environmental temperature.

As an alternative procedure, Mori–Tanaka mean field scheme can be applied to evaluate the locally effective material properties (see Ref. 12).

Equations of Motion and Boundary Conditions

To derive the equations of motion of rotating tapered pretwisted functionally graded blades and the associated boundary conditions, the extended Hamilton's principle is used. This can be formulated as

$$\int_{t_1}^{t_2} (\delta\mathcal{K} - \delta V + \delta W)\,\mathrm{d}t = 0$$

$$\delta u_0 = \delta v_0 = \delta\theta_x = \delta\theta_y = 0 \qquad \text{at } t = t_1, t_2 \tag{21}$$

where $\mathcal{K}$ and V are the kinetic and strain energy, respectively, δW is the virtual work of external forces, t_1 and t_2 are two arbitrary instants of time, and δ is the variation operator.

With Eqs. (3) and (7) in mind, in light of Hamilton's condition (21), for the problem at hand that involves the bending–bending–transverse shear coupling, one obtains

$$\int_{t_0}^{t_1} \delta\mathcal{K}\,\mathrm{d}t = \int_{t_0}^{t_1} \left\{ \int_0^L -\left\{ b_1\left(\ddot{u}_0 - \underline{\underline{u_0\Omega^2}}\right)\delta u_0 + b_1\ddot{v}_0\delta v_0 \right.\right.$$

$$+ (b_5 + \delta_n b_{15})\left(\ddot{\theta}_y - \underline{\underline{\Omega^2\theta_y}}\right)\delta\theta_y$$

$$\left.\left. + \left[(b_4 + \delta_n b_{14})\left(\ddot{\theta}_x - \underline{\underline{\Omega^2\theta_x}}\right)\right]\delta\theta_x \right\}\mathrm{d}z \right\}\mathrm{d}t \tag{22}$$

where the reduced mass terms b_i are supplied in the Appendix. In addition, in Eq. (22) and next equations, the terms underscored by dotted lines belong to rotatory inertia. For the variation of the strain energy δV one obtains[17]

$$\int_{t_0}^{t_1}\int_\tau \sigma_{ij}\delta\varepsilon_{ij}\,\mathrm{d}\tau\,\mathrm{d}t = \int_{t_0}^{t_1}\int_0^L -\{(M_y' - Q_x)\delta\theta_y + (M_x' - Q_y)\delta\theta_x$$

$$+ [Q_x' + (T_z u_0')']\delta u_0 + [Q_y' + (T_z v_0')']\delta v_0\}\,\mathrm{d}z\,\mathrm{d}t$$

$$+ \int_{t_0}^{t_1} [M_y\delta\theta_y + M_x\delta\theta_x + (Q_x + T_z u_0')\delta u_0$$

$$+ (Q_y + T_z v_0')\delta v_0]_0^L\,\mathrm{d}t \tag{23}$$

These equations are supplied in terms of one-dimensional stress resultants, T_z, Q_x, and Q_y, that denote the axial and the shear forces in the x and y directions, respectively, and stress couples M_x and M_y about the x and y axes, respectively. Their expressions are as follows:

$$T_z(z;t) = \oint N_{zz}\,\mathrm{d}s \tag{24a}$$

$$M_y(z;t) = \oint \left(xN_{zz} + L_{zz}\frac{\mathrm{d}y}{\mathrm{d}s}\right)\mathrm{d}s \tag{24b}$$

$$M_x(z;t) = \oint \left(yN_{zz} - L_{zz}\frac{\mathrm{d}x}{\mathrm{d}s}\right)\mathrm{d}s \tag{24c}$$

$$Q_x(z;t) = \oint \left(N_{sz}\frac{\mathrm{d}x}{\mathrm{d}s} + L_{zn}\frac{\mathrm{d}y}{\mathrm{d}s}\right)\mathrm{d}s \tag{24d}$$

$$Q_y(z;t) = \oint \left(N_{sz}\frac{\mathrm{d}y}{\mathrm{d}s} - L_{zn}\frac{\mathrm{d}x}{\mathrm{d}s}\right)\mathrm{d}s \tag{24e}$$

where $\oint(\cdot)\,\mathrm{d}s$ denotes the integral along the beam midline contour.

The virtual work of external forces is expressed as

$$\delta W = \int_0^L [p_x\delta u_0 + p_y\delta v_0 + m_x\delta\theta_x + m_y\delta\theta_y]\,\mathrm{d}z$$

$$+ [\underset{\sim}{Q}_x\delta u_0 + \underset{\sim}{Q}_y\delta v_0 + \underset{\sim}{M}_x\delta\theta_x + \underset{\sim}{M}_y\delta\theta_y]|_0^L \tag{25}$$

where p_x and p_y are the distributed loads in the spanwise direction, m_x and m_y are the distributed moments about the axes x and y, respectively, and the terms underscored by tildes denote prescribed quantities. For the problem considered here, these latter terms are discarded. Using Eqs. (22–25) in the extended Hamilton's principle, Eq. (21), invoking the stationarity of the functional in the time interval $[t_0, t_1]$, and having in view that the variations $(\delta u_0, \delta v_0, \delta\theta_x, \delta\theta_y)$ are independent and arbitrary, their coefficients in the two integrands must vanish independently. This yields the equations of motion and the boundary conditions, which are not displayed here. Integrating the three-dimensional constitutive equations (12) through the beam thickness and postulating that the hoop stress resultant N_{ss} is negligibly small when compared with the remaining ones, two-dimensional constitutive equations relating the stress resultants N_{zz}, N_{sz}, and N_{zn} and stress couples L_{zz} and L_{sz} with the strain measures defined by Eqs. (8–11) are obtained. These are referred to as shell-constitutive equations. Replacement of the obtained two-dimensional constitutive equations in Eqs. (24) results in the following form of one-dimensional constitutive equations

$$\begin{bmatrix} M_y \\ M_x \\ Q_x \\ Q_y \end{bmatrix} = \begin{bmatrix} a_{22} & a_{23} & 0 & 0 \\ a_{32} & a_{33} & 0 & 0 \\ 0 & 0 & a_{44} & a_{45} \\ 0 & 0 & a_{54} & a_{55} \end{bmatrix} \begin{bmatrix} \theta_y' \\ \theta_x' \\ u_0' + \theta_y \\ v_0' + \theta_x \end{bmatrix} + \begin{bmatrix} M_y^T \\ M_x^T \\ 0 \\ 0 \end{bmatrix} \tag{26}$$

In these equations, $a_{ij}(=a_{ji})$ are stiffness coefficients and M_y^T and M_x^T are one-dimensional thermal moment terms. Their expressions are displayed in the Appendix. Notice that for the nonuniform cross sections and/or pretwisted beams, $a_{ij} \to a_{ij}(z)$.

Application of Hamilton's principle yields the governing equations featuring the bending (flapping)–bending (lagging) transverse shear coupling that are expressed as

$$\delta u_0 : [a_{44}(z)(u_0' + \theta_y) + a_{45}(z)(v_0' + \theta_x)]'$$

$$- b_1\ddot{u}_0 + \underline{\underline{b_1 u_0\Omega^2}} + \underline{\underline{\Omega^2[R(z)u_0']'}} + p_x = 0 \tag{27a}$$

$$\delta v_0 : [a_{55}(z)(v_0' + \theta_x) + a_{54}(z)(u_0' + \theta_y)]'$$

$$- b_1\ddot{v}_0 + \underline{\underline{\Omega^2[R(z)v_0']'}} + p_y = 0 \tag{27b}$$

$$\delta\theta_y : \left[a_{22}(z)\theta_y' + a_{23}(z)\theta_x'\right]' - a_{44}(z)(u_0' + \theta_y) - a_{45}(z)(v_0' + \theta_x)$$

$$- (b_5(z) + \delta_n b_{15}(z))\left(\ddot{\theta}_y - \underline{\underline{\Omega^2\theta_y}}\right)$$

$$- (b_6(z) - \delta_n b_{13}(z))\left(\ddot{\theta}_x - \underline{\underline{\Omega^2\theta_x}}\right) + m_y = \left(M_y^T\right)' \tag{27c}$$

$$\delta\theta_x : [a_{33}(z)\theta_x' + a_{32}(z)\theta_y']'$$

$$- a_{55}(z)(v_0' + \theta_x) - a_{54}(z)(u_0' + \theta_y)$$

$$- (b_4(z) + \delta_n b_{14}(z))\left(\ddot{\theta}_x - \underline{\underline{\Omega^2\theta_x}}\right)$$

$$- (b_6(z) - \delta_n b_{13}(z))\left(\ddot{\theta}_y - \underline{\underline{\Omega^2\theta_y}}\right) + m_x = \left(M_x^T\right)' \tag{27d}$$

In these equations p_x, p_y, m_x, and m_y are the external loads and moments that are assumed to be functions of both the spanwise and time coordinates, $b_i(z)$ are reduced mass terms, whose expressions are provided by Eqs. (A4), and δ_n is a tracer that takes the values 1 or 0, depending on whether the effects off the midline contour are taken into consideration or discarded, respectively. Assuming the blade to be clamped at $z = 0$ and free at $z = L$, the corresponding boundary conditions are at $z = 0$

$$u_0 = v_0 = \theta_y = \theta_x = 0 \tag{28}$$

and at $z = L$

$$\delta u_0 : a_{44}(L)(u_0' + \theta_y) + a_{45}(L)(v_0' + \theta_x) = 0 \tag{29a}$$

$$\delta v_0 : a_{55}(L)\ (v_0' + \theta_x) + a_{54}(L)(u_0' + \theta_y) = 0 \tag{29b}$$

$$\delta\theta_y : a_{22}(L)\theta_y' + a_{23}(L)\theta_x' = M_y^T(L) \tag{29c}$$

$$\delta\theta_x : a_{33}(L)\theta_x' + a_{32}(L)\theta_y' = M_x^T(L) \tag{29d}$$

These equations can address the static and dynamic response of rotating blades exposed to external thermomechanical excitation or the free-vibration problem.

In these equations, paralleling the procedure used in Ref. 17, one obtains

$$R(z) = -\int_L^z b_1(z)(R_0 + z)\,\mathrm{d}z \tag{30a}$$

that in the case of a uniform blade becomes

$$R(z) = b_1\left[R_0(L - z) + \tfrac{1}{2}(L^2 - z^2)\right] \tag{30b}$$

A cursory inspection of the expression of stiffness quantities a_{ij} (Appendix) reveals that, for non-pretwisted blades, that is, when $M = 1$ and $N = 0$, and also for doubly symmetric blade cross sections, the coupling stiffnesses a_{45} and a_{23} and the mass terms b_6 and b_{13} become immaterial. In these cases, the decoupling between flapping and lagging takes place.

Bernoulli–Euler Counterpart System

Extracting the expressions $a_{44}(u_0' + \theta_y) + a_{45}(v_0' + \theta_x)$ and $a_{55}(v_0' + \theta_x) + a_{54}(u_0' + \theta_y)$ from Eqs. (27c) and (27d), respectively, and their corresponding replacement in Eqs. (27a), (27b), (29a), and (29b), followed by consideration of $\theta_x \to -v_0'$ and $\theta_y = -u_0'$ yields the Bernoulli–Euler counterpart of the shearable beam model.

As a result, the governing equations read

$$\delta u_0 : [a_{22}(z)u_0'' + a_{23}(z)v_0'']'' - \left\{[b_5(z) + \delta_n b_{15}(z)]\left(\ddot{u}_0' - \underline{\underline{\Omega^2 u_0'}}\right)\right.$$
$$\left. + [b_6(z) - \delta_n b_{13}(z)]\left(\ddot{v}_0' - \underline{\underline{\Omega^2 v_0'}}\right)\right\}' + b_1\ddot{u}_0 - \underline{\underline{b_1\Omega^2 u_0}}$$
$$- \underline{\underline{\Omega^2[R(z)u_0']'}} - p_x - m_y' + \left(M_y^T\right)'' = 0 \tag{31a}$$

$$\delta v_0 : [a_{33}(z)v_0'' + a_{32}(z)u_0'']'' - \left\{[b_4(z) + \delta_n b_{14}(z)]\left(\ddot{v}_0' - \underline{\underline{\Omega^2 v_0'}}\right)\right.$$
$$\left. + [b_6(z) - \delta_n b_{13}(z)]\left(\ddot{u}_0' - \underline{\underline{\Omega^2 u_0'}}\right)\right\}' + b_1\ddot{v}_0 - \underline{\underline{\Omega^2[R(z)v_0']'}}$$
$$- p_y - m_x' + \left(M_x^T\right)'' = 0 \tag{31b}$$

The associated homogeneous boundary conditions at $z = 0$ are

$$u_0 = v_0 = u_0' = v_0' = 0 \tag{32}$$

and at $z = L$ are

$$\delta u_0 : [a_{22}(L)u_0'' + a_{23}(L)v_0'']' - [b_5(L) + \delta_n b_{15}(L)]\left(\ddot{u}_0' - \underline{\underline{\Omega^2 u_0'}}\right)$$
$$- [b_6(L) - \delta_n b_{13}(L)]\left(\ddot{v}_0' - \underline{\underline{\Omega^2 v_0'}}\right) - m_y(L) + \left(M_y^T\right)'(L) = 0 \tag{33a}$$

$$\delta v_0 : [a_{33}(L)v_0'' + a_{32}(L)u_0'']' - [b_4(L) + \delta_n b_{14}(L)]\left(\ddot{v}_0' - \underline{\underline{\Omega^2 v_0'}}\right)$$
$$- [b_6(L) - \delta_n b_{13}(L)]\left(\ddot{u}_0' - \underline{\underline{\Omega^2 u_0'}}\right) - m_x(L) + \left(M_x^T\right)'(L) = 0 \tag{33b}$$

$$\delta u_0' : a_{22}(L)u_0'' + a_{23}(L)v_0'' = 0 \tag{33c}$$

$$\delta v_0' : a_{33}(L)v_0'' + a_{32}(L)u_0'' = 0 \tag{33d}$$

Validation of the Model Against a Few Results from the Literature

Based on the displayed governing equations, the static response of FGM blades to external loads and temperature gradients and/or the dynamic response to time-dependent loads and the free-vibration problem can be studied.

Note that the equations derived for rotating tapered pretwisted thin-walled beams are similar to the ones corresponding to a solid beam. The difference occurs only in the proper expression of cross-sectional stiffness and mass terms. To validate the present model, comparisons with a number of results available in the literature that have been carried out by using a solid beam model are presented in Table 1 (Refs. 22–24). For the Timoshenko beam model these are considered:

$$\frac{b_4[0] + \delta_n b_{14}[0]}{b_1[0]L^2} = 0.0064, \qquad \frac{a_{33}[0]}{a_{55}[0]L^2} = 0.01958$$

and for the Bernoulli–Euler one:

$$\frac{b_4[0] + \delta_n b_{14}[0]}{b_1[0]L^2} = 0, \qquad \frac{a_{33}[0]}{a_{55}[0]L^2} = 0$$

Table 1 Comparisons of dimensionless flapping natural frequencies for a tapered untwisted rotating beam[a]

	Timoshenko		Bernoulli–Euler			
$\bar{\omega}_i$	Ref. 22	Present	Ref. 22	Ref. 23	Ref. 24	Present
			$\bar{\Omega} = 0$			
$\bar{\omega}_1$	3.6500	3.6499	3.8238	3.8238	3.8242	3.8238
$\bar{\omega}_2$	15.022	15.022	18.317	18.317	18.320	18.317
$\bar{\omega}_3$	32.785	32.784	47.265	47.264	47.271	47.274
$\bar{\omega}_4$	53.341	53.379	90.450	——	——	91.865
			$\bar{\Omega} = 3$			
$\bar{\omega}_1$	4.8866	4.8865	5.0927	5.0927	5.0927	5.0927
$\bar{\omega}_2$	16.460	16.460	19.684	19.684	19.684	19.684
$\bar{\omega}_3$	34.458	34.457	48.619	48.619	48.620	48.629
$\bar{\omega}_4$	55.358	55.395	91.822	——	——	93.201
			$\bar{\Omega} = 5$			
$\bar{\omega}_1$	6.4712	6.4711	6.7434	6.7345	6.7432	6.7434
$\bar{\omega}_2$	18.744	18.744	21.905	21.905	21.905	21.906
$\bar{\omega}_3$	37.224	37.223	50.934	50.934	49.646	50.945
$\bar{\omega}_4$	58.730	58.744	94.206	——	——	95.529
			$\bar{\Omega} = 10$			
$\bar{\omega}_1$	10.991	10.991	11.502	11.502	11.501	11.502
$\bar{\omega}_2$	26.928	26.928	30.183	30.183	30.177	30.183
$\bar{\omega}_3$	47.883	47.884	60.564	60.564	60.555	60.582
$\bar{\omega}_4$	71.989	72.020	104.61	——	——	105.72

[a]Here $\alpha_c = 0.5$, $\alpha_h = 1$, $R_0 = 0$, $\lambda = 0$, and $\beta_0 = 0$.

The comparisons concern the free vibration problem of a chordwise tapered rotating blade. The blade material is assumed to be isotropic and the temperature effects are discarded.

In Table 1, the following dimensionless parameters have been considered:

$$\bar{\omega}_i^4 = \frac{b_1[0]L^4}{a_{33}[0]}\omega^2, \qquad \bar{\Omega}^2 = \frac{b_1[0]L^2}{a_{33}[0]}\Omega^2$$

$$\frac{a_{55}[\eta]}{a_{55}[0]} = \frac{b_1[\eta]}{b_1[0]} = 1 - \alpha_c\eta$$

$$\frac{b_4[\eta] + b_{14}[\eta]}{b_4[0] + b_{14}[0]} = \frac{a_{33}[\eta]}{a_{33}[0]} = (1 - \alpha_c\eta)^3$$

The comparisons concern both the shearable and the classical model counterpart, and in both cases, very good agreement was reached. Note that the predictions in Ref. 22 have been obtained via the finite element method.

Numerical Simulations and Discussion

Numerical simulations concern the free-vibration problem of FGM rotating blades. To obtain the eigenvalue problem whose solution will provide the natural frequencies and mode shapes, the

Table 2 Material properties of FGM constituents

Material properties	P_0	P_1	P_1	P_2	P_3	P^a
E, N/m^2						
SN	348.43×10^9	0	-3.070×10^{-4}	2.160×10^{-7}	-8.946×10^{-11}	322.2715×10^9
SS	201.04×10^9	0	3.079×10^{-4}	-6.534×10^{-7}	0	207.7877×10^9
ν						
SN	0.2400	0	0	0	0	0.2400
SS	0.3262	0	-2.002×10^{-4}	3.797×10^{-7}	0	0.31776
ρ, kg/m^3						
SN	2370	0	0	0	0	2370
SS	8166	0	0	0	0	8166

[a]Properties are evaluated at $T = 300$ K.

unknown one-dimensional displacement quantities are represented in a generic form as

$$[u_0(z;t), v_0(z;t), \theta_x(z;t), \theta_y(z;t)] = [U(z), V(z), S(z), P(z)] \exp(i\omega t) \tag{34}$$

where ω is the eigenfrequency and the spatial parts are expressed as

$$[U(z), V(z), S(z), P(z)] = \sum_{j=1}^{n} [a_j u_j(z), b_j v_j(z), c_j s_j(z), d_j p_j(z)] \tag{35}$$

In Eq. (35), $u_j(z)$, $v_j(z)$, $s_j(z)$, and $p_j(z)$ are the trial functions selected to fulfil the boundary conditions.

However, in the spirit of the extended Galerkin method (EGM) applied here (see Refs. 25 and 26), only admissible functions, that is, trial functions exactly fulfilling the geometrical boundary conditions, are used. As a result, the trial functions are represented as polynomials of various powers with respect to the spanwise coordinate z. Consistent with EGM, representation (34) in conjunction with Eq. (35) are inserted in Hamilton's functional. Because only the dynamic boundary conditions are not fulfilled, these remain in the functional as residual terms, together with the ones resulting from the equations of motion, and are minimized in the Galerkin's sense.

For the problem at hand, the eigenvalue problem results in the standard form

$$\boldsymbol{A}\boldsymbol{x} = \omega^2 \boldsymbol{x}, \qquad \boldsymbol{A} = \boldsymbol{M}^{-1}\boldsymbol{K} \tag{36}$$

where $\boldsymbol{M}$ and $\boldsymbol{K}$ are the mass and stiffness $4n \times 4n$ matrices; $\boldsymbol{x}^T = [a_1, a_2, \ldots, a_n, b_1, b_2, \ldots, b_n, c_1, c_2, \ldots, c_n, d_1, d_2, \ldots, d_n]$. As previously shown,[26] the EGM provides excellent accuracy of the solution as well as rapid convergence.

The turbine blade is modeled as a tapered thin-walled beam of rectangular cross section with geometric characteristics $R_0 = 1.3$ m, $L = 1.52$ m, $c_R = 0.257$ m, $b_R = 0.0827$ m, and $h = 0.01654$ m. Moreover, it is made up of FGMs constituted of two distinct material phases, that is, of a ceramic, silicon nitride (SN), and a metal, stainless steel (SS), featuring temperature-dependent properties. The material properties, denoted generically as P, can be expressed as a function of temperature as in Eqs. (14). For the two basic constituents, the coefficients P_i are provided in Table 2.

Figure 2 shows the variation of bending stiffness quantities a_{22} and $0.1a_{33}$, as a function of the volume fraction parameter, for two values of the temperature gradient λ [see Eq. (18b)]. Note that the bending stiffnesses a_{22} and a_{33} decrease with the increase of K from $K = 0$ (full ceramic) toward $K = 10$ (full metal). This trend is stronger in the case of larger temperature gradients, such as $\lambda = 5$, than in that of the uniform through the blade thickness temperature distribution, $\lambda = 0$. Therefore, the proper selection of K can lead to the increase of bending stiffness.

Figures 3 and 4 show for the case of nonpretwisted and nonrotating blades the variations of the first and second decoupled natural frequencies in flapping and lagging, against the temperature gradient, for selected values of the volume fraction parameter K.

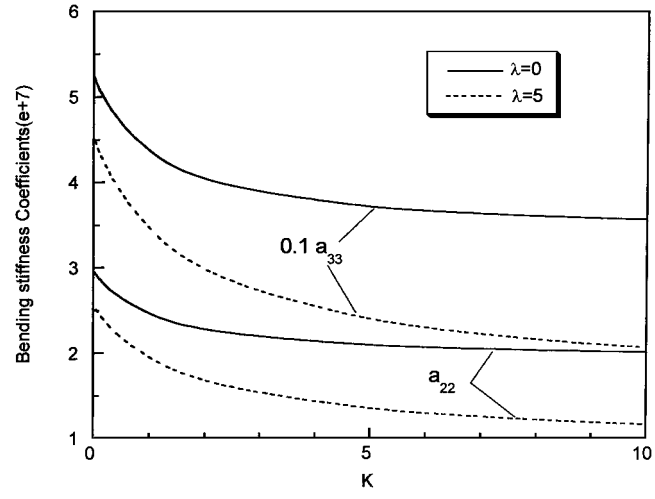

Fig. 2 Variation of bending stiffness quantities with that of the volume fraction parameter K, for two selected values of λ, where $\alpha_c = \alpha_h = 1$.

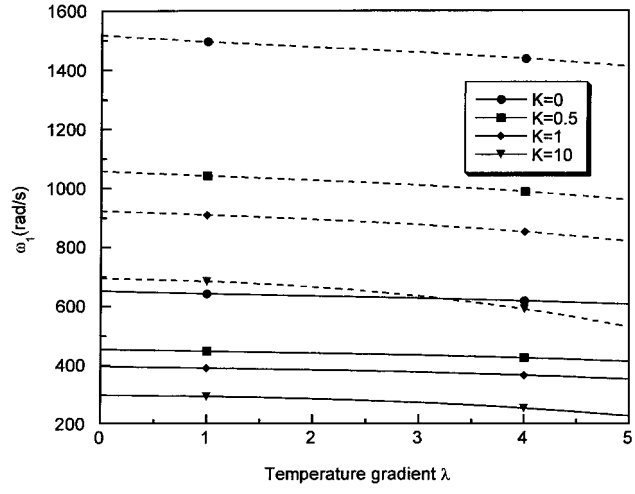

Fig. 3 First decoupled flapping and lagging natural frequencies with temperature gradient for selected values of the volume fraction parameter ($\beta_0 = \Omega = 0$ and $\alpha_c = \alpha_h = 1.2$): ——, ω_{F_1} and – – –, ω_{L_1}.

As a general trend, the increase of the thermal gradient λ results in a decay of eigenfrequencies. This trend is stronger for the lagging frequencies than for the flapping ones. However, the strongest variation is due to the variation of the volume fraction parameter K. In this sense, the eigenfrequencies are largest in the case of ceramic blades and decay with the increase of K toward full metallic blades.

The variation of the first two coupled bending-bending natural frequencies, occurring in the case of pretwisted rotating blades vs. the rotational speed is shown in Figs. 5 and 6. The results reveal a similar trend of variation of natural frequencies with respect to the variation of K and λ to the case of decoupled natural frequencies.

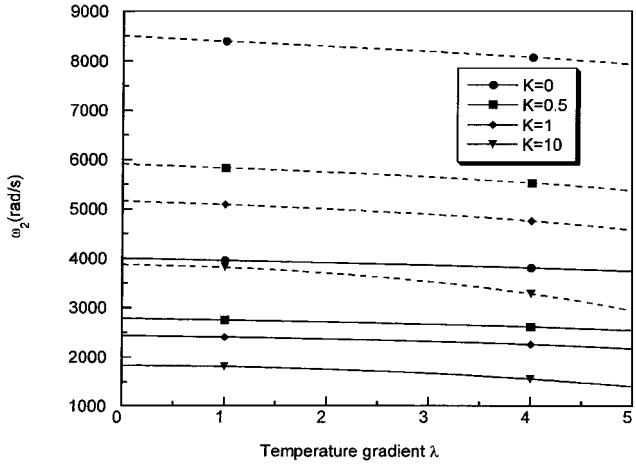

Fig. 4 Counterpart of Fig. 3 for the second decoupled flapping and lagging natural frequencies ($\beta_0 = \Omega = 0$, and $\alpha_c = \alpha_h = 1.2$): ——, ω_{F_2} and – – –, ω_{L_2}.

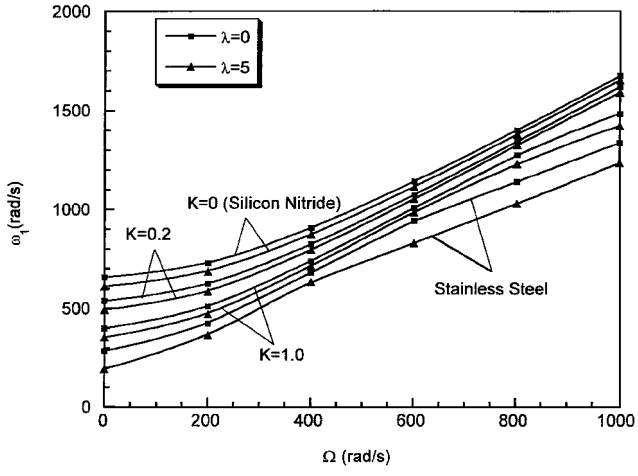

Fig. 5 First flapping–lagging natural frequency vs rotational speed for selected values of the parameter K and two values of λ ($\beta_0 = 58$ deg and $\alpha_c = \alpha_h = 1.2$).

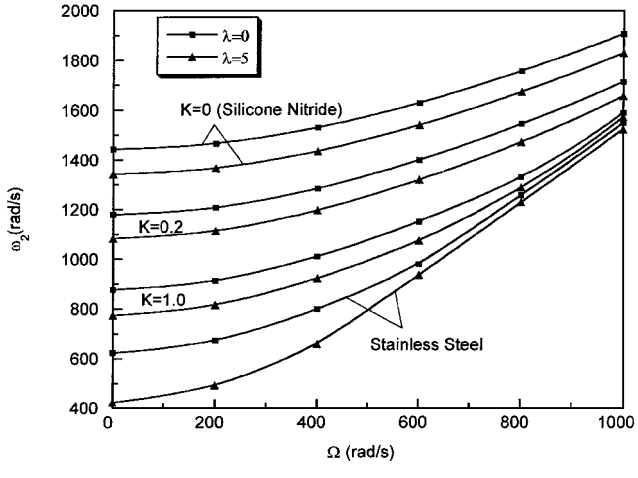

Fig. 6 Counterpart of Fig. 5 for the second coupled natural frequency.

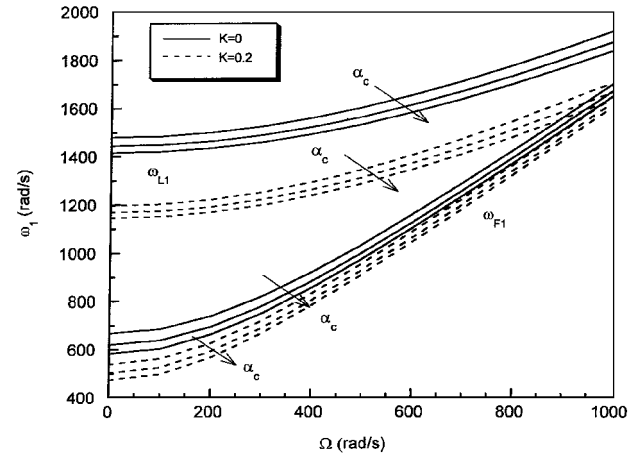

Fig. 7 First decoupled flapping and lagging natural frequency vs rotational speed for selected chord taper ratios, $\alpha_c = 0.7$, 1, and 1.3, and two values of the parameter K ($\beta_0 = 0$, $\alpha_h = 1$, and $\lambda = 5$).

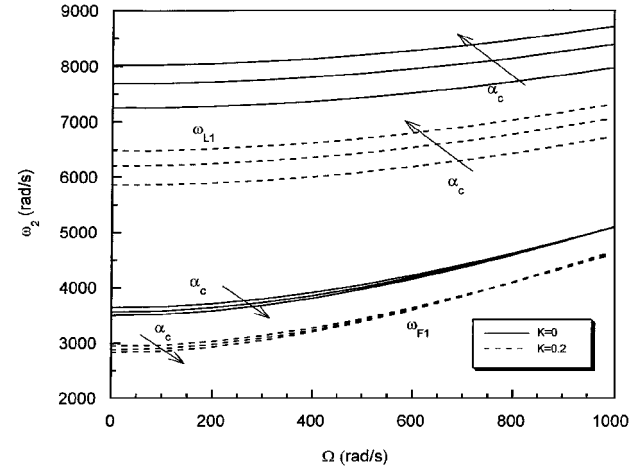

Fig. 8 Counterpart of Fig. 7 for the second decoupled flapping and lagging natural frequency ($\beta_0 = 0$, $\alpha_h = 1$, and $\lambda = 5$).

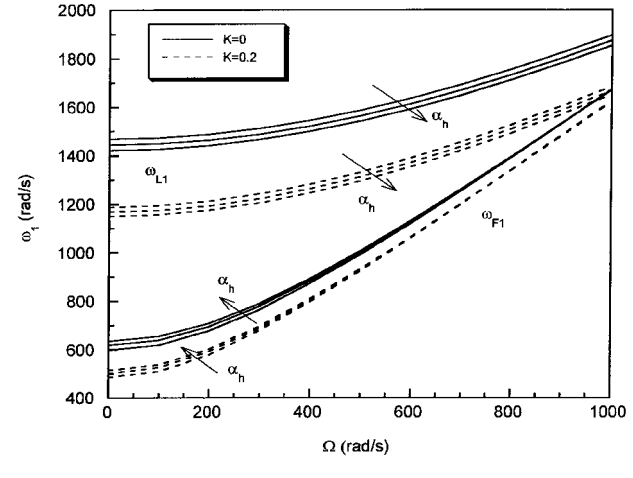

Fig. 9 First decoupled flapping and lagging natural frequency vs rotational speed for various height taper ratios, $\alpha_h = 0.7$, 1, and 1.3, and two values of the parameter K ($\beta_0 = 0$, $\alpha_c = 1$, and $\lambda = 5$).

However, as revealed in Figs. 3–6, the strongest decay of natural frequencies with the increase of λ occurs for increased values of K approaching the metallic blade. Throughout these plots, the stiffening effect induced by the centrifugal forces is manifested by the increase of natural frequencies with the increase of Ω.

In Figs. 7 and 8, for the case of the tapered blades without pretwist and for $K = 0$ and 0.2, the variations of lagging and flapping natural frequencies with the rotational speed are shown. The results related to the variation of the lagging and flapping frequencies with the rotational speed reveal a well-known general trend.[17] In addition, the results reveal that, for the first natural frequencies, for tapers $\alpha_c < 1$, an increase of eigenfrequencies in lagging and flapping as compared to $\alpha_c \geq 1$ results. However, for the flapping frequencies, this trend tends to be attenuated with the increase of Ω. For the second frequencies in flapping and lagging, a more complex variation with the chord taper ratio is experienced.

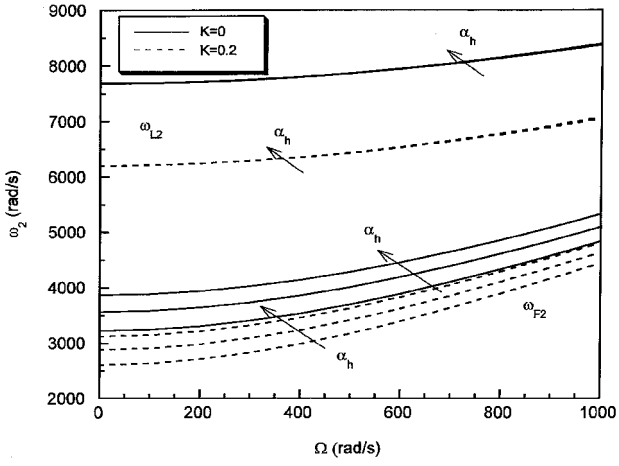

Fig. 10 Counterpart of Fig. 9 for the second decoupled flapping and lagging natural frequencies ($\beta_0 = 0$, $\alpha_c = 1$, and $\lambda = 5$).

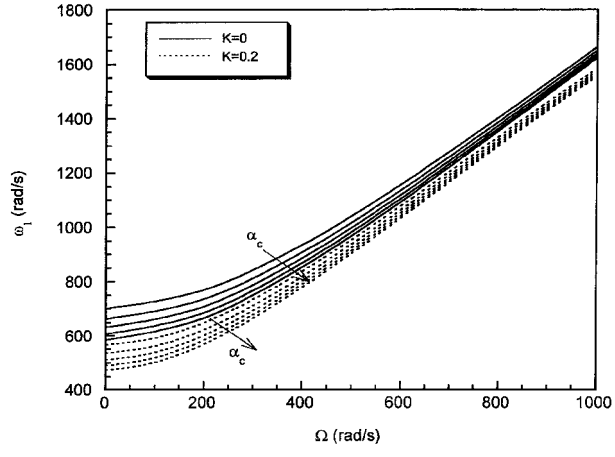

Fig. 11 First natural frequency vs rotational speed for various chord taper ratios, $\alpha_c = 0.6, 0.8, 1, 1.2,$ and 1.4, and two values of the parameter K ($\beta = 90$ deg, $\alpha_h = 1$, and $\lambda = 5$).

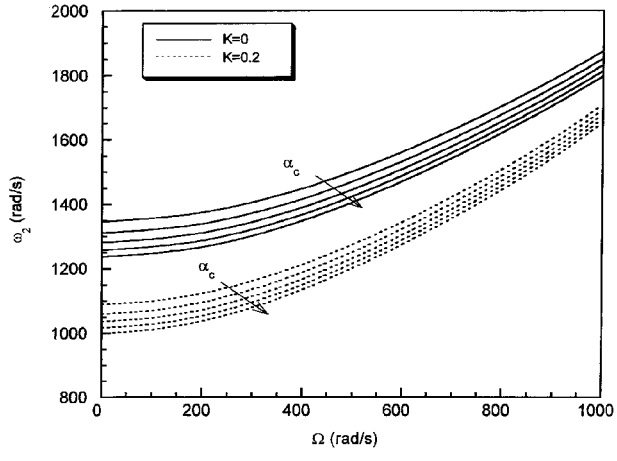

Fig. 12 Counterpart of Fig. 11 for the second natural frequency.

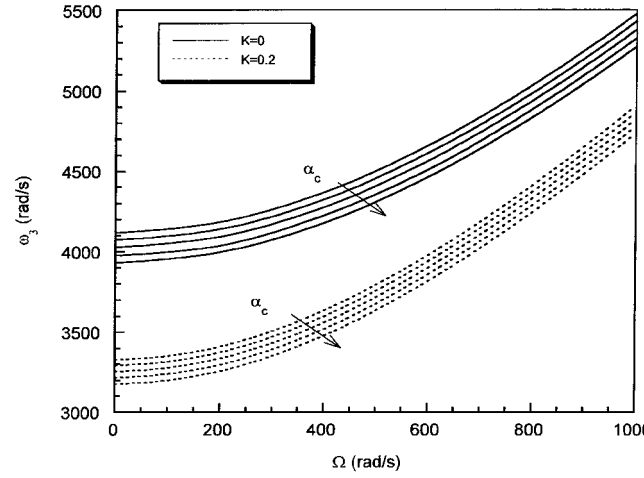

Fig. 13 Counterpart of Fig. 11 for the third natural frequency.

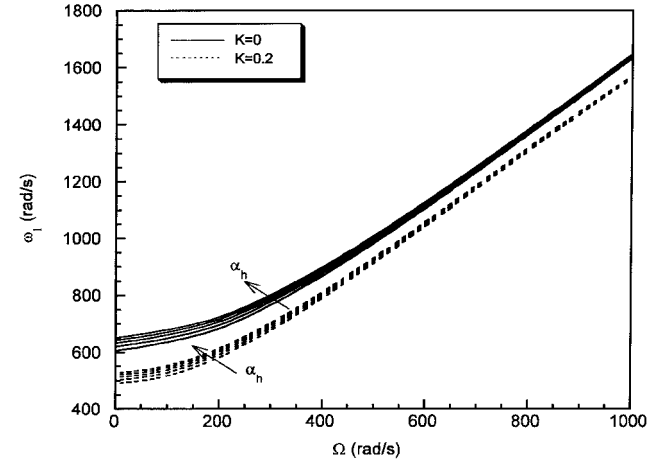

Fig. 14 First natural frequency vs rotational speed for various height taper ratios, $\alpha_h = 0.6, 0.8, 1, 1.2,$ and 1.4, and two values of the parameter K ($\beta = 90$ deg, $\alpha_c = 1$, and $\lambda = 5$).

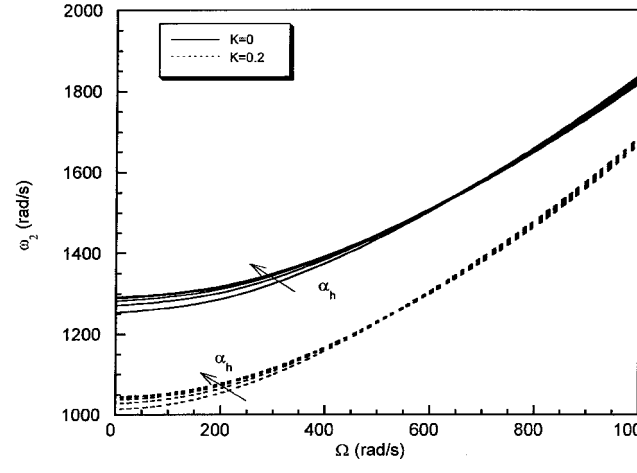

Fig. 15 Counterpart of Fig. 14 for the second natural frequency.

For the uniform/tapered blades corresponding to $\alpha_c \geq 1$, the lagging frequencies are larger than those corresponding to $\alpha_c < 1$, a trend that occurs irrespective of the rotational speed. At the same time, at relatively lower rotational speeds, the flapping frequencies for tapers $\alpha_c \leq 1$ are slightly larger than the ones corresponding to $\alpha_c > 1$, a trend that is reversed once Ω is increasing.

In Figs. 9 and 10, the effect of the height-taperratio α_h on flapping and lagging frequencies is shown. As is readily seen from Figs. 9 and 10, the trend of variation with α_h is more complex than in the case of the variation with α_c. Note that the second flapping frequency is more affected by the variation of α_h than its lagging frequency counterpart.

In all considered cases related to the effect of the chord taper ratio α_c on the coupled bending–bending frequencies of pretwisted FGM blades (Figs. 11–13), it was shown that the chord taper $\alpha_c \leq 1$ has a more beneficial influence on coupled frequencies than $\alpha_c > 1$, a trend that occurs at any Ω. An oppositeeffect (Figs. 14–16) is played by the

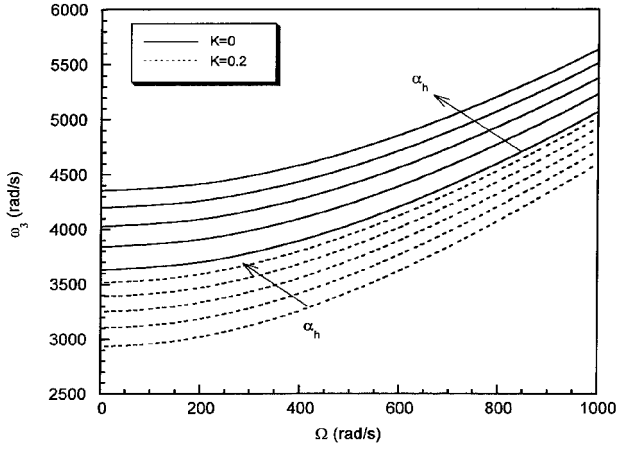

Fig. 16 Counterpart of Fig. 14 for the third natural frequency.

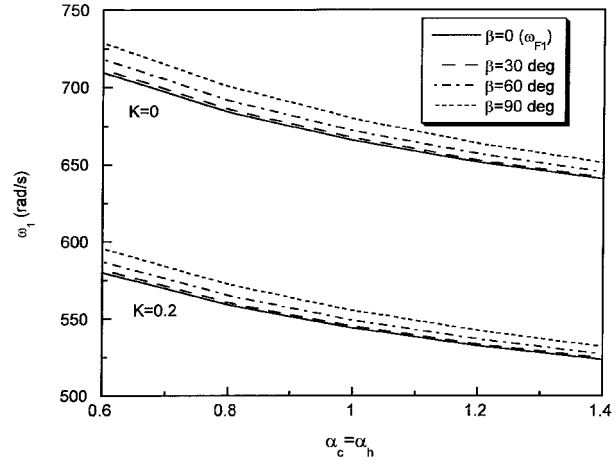

Fig. 17 Variation of the first natural frequency vs taper ratio for selected values of the pretwist angle and for $K = 0$ and 0.2 ($\Omega = 0$ and $\lambda = 0$), for $\beta_0 = 0 \Rightarrow \omega_1 = \omega_{F_1}$.

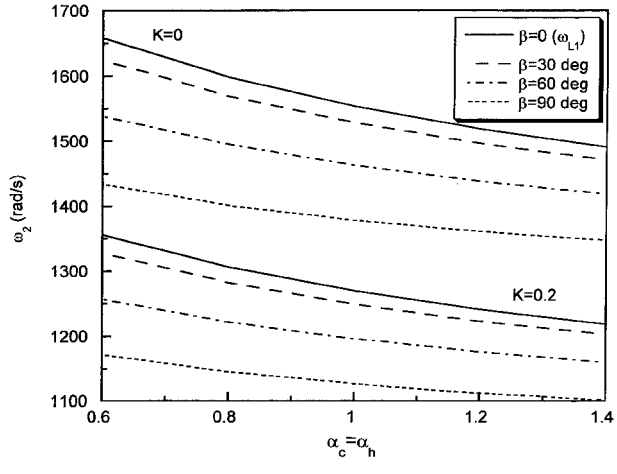

Fig. 18 Counterpart of Fig. 17 for the second natural frequency (for $\beta_0 = 0 \Rightarrow \omega_2 = \omega_{L_1}$).

height taper, in the sense that the tapered blades $\alpha_h \geq 1$ experience larger natural frequencies than those characterized by $\alpha_h < 1$.

The effect of pretwist coupled with that of taper on the FGM nonrotating blades is shown in Figs. 17–19. It is seen that the pretwist plays an alternating effect on the natural frequencies, in that for the odd mode frequencies the increase of the pretwist is beneficial, whereas for the even mode frequencies the increase is detrimental. On the other hand, with the simultaneous increase of the taper in

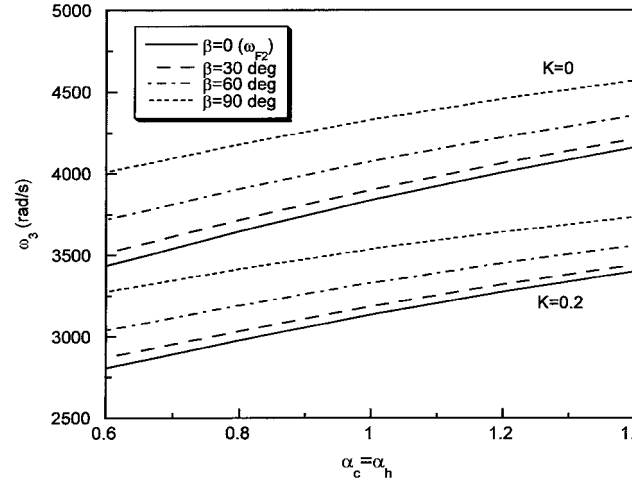

Fig. 19 Counterpart of Fig. 17 for the third natural frequency (for $\beta_0 = 0 \Rightarrow \omega_3 = \omega_{F_2}$).

chord and height, the first two coupled natural frequencies decrease for $\alpha_c (= \alpha_h) > 1$ and increase for $\alpha_c (= \alpha_h) < 1$, whereas for the third coupled natural frequency, an opposite trend related to the effect of the taper is experienced.

Throughout these results, it was revealed that the increase of the volume fraction parameter K yields, invariably, a decrease of natural frequencies.

Conclusions

A study devoted to the modeling and vibration of functionally graded rotating blades featuring bending–bending–transverse shear elastic coupling and operating in a high-temperature environment has been presented. The blade was modeled as a pretwisted thin-walled beam of nonuniform cross sections that also includes the transverse shear effect.

The material properties of the FGM are assumed to vary through the blade thickness in accordance to a power law. It was shown that the gradients in the material properties, the constituent volume fractions, considered in conjunction with the temperature gradient significantly affect the free-vibration characteristics of rotating blades. Moreover, proper consideration of the volume fraction of the constituent materials can provide an optimized design from the free-vibration point of view. In the same context, the influence of the blade taper ratios α_c and α_h on natural frequencies was highlighted.

Note that the obtained equations are general, in the sense that, based on them, static and dynamic response analyses of FGM rotating blades can be carried out.

Appendix: Expressions of Stiffness and Mass Terms

$$K_{11} = A_{11} - \left(A_{12}^2 / A_{11}\right) \tag{A1a}$$

$$K_{22} = A_{66} \tag{A1b}$$

$$K_{14} = K_{41} = B_{11} - (A_{12}B_{12}/A_{11}) \tag{A1c}$$

$$K_{23} = 2A_{66}(A_c/C) \tag{A1d}$$

where A_c and C are the beam cross-sectional area bordered by the midline contour and its total length, respectively, and A_{ij}, B_{ij}, and D_{ij} are the shell-stiffnesses in stretching, coupled bending–stretching, and bending, respectively. In addition,

$$\hat{N}_{zz}^T(s, z) = [1 - (A_{12}/A_{11})]N_{zz}^T \tag{A2a}$$

$$\hat{L}_{zz}^T = L_{zz}^T - (B_{12}/A_{11})N_{zz}^T \tag{A2b}$$

where

$$\left(N_{zz}^T, L_{zz}^T\right) = \int_{-h/2}^{h/2} \Delta T(Q_{11} + Q_{12})\hat{\alpha}(1, n)\,\mathrm{d}n \tag{A2c}$$

and the one-dimensional thermal loading terms are given by

$$M_x^T(z) = \oint \left[y\hat{N}_{zz}^T - \frac{\mathrm{d}x}{\mathrm{d}s}\hat{L}_{zz}^T \right] \mathrm{d}s$$

$$M_y^T(z) = \oint \left[x\hat{N}_{zz}^T + \frac{\mathrm{d}y}{\mathrm{d}s}\hat{L}_{zz}^T \right] \mathrm{d}s$$

These terms play the role of bending moments about the axes x and y, respectively. The one-dimensional stiffness quantities are defined as

$$\begin{aligned}
a_{44}(z) &= M^2 a_{44}^p(z) + N^2 a_{55}^p(z) - 2MN a_{45}^p(z) \\
a_{23}(z) &= MN\left[a_{22}^p(z) - a_{33}^p(z)\right] \\
a_{22}(z) &= M^2 a_{22}^p(z) + N^2 a_{33}^p(z) - 2MN a_{23}^p(z) \\
a_{33}(z) &= M^2 a_{33}^p(z) + N^2 a_{22}^p(z) + 2MN a_{23}^p(z) \\
a_{45}(z) &= MN\left[a_{44}^p(z) - a_{55}^p(z)\right] \\
a_{55}(z) &= M^2 a_{55}^p(z) + N^2 a_{44}^p(z) + 2MN a_{54}^p(z)
\end{aligned} \tag{A3}$$

$$a_{22}^p = \oint \left[K_{11}x^2 + K_{44}\left(\frac{\mathrm{d}y}{\mathrm{d}s}\right)^2 \right] \mathrm{d}s$$

$$a_{33}^p = \oint \left[K_{11}y^2 + K_{44}\left(\frac{\mathrm{d}x}{\mathrm{d}s}\right)^2 \right] \mathrm{d}s$$

$$a_{44}^p = \oint \left[K_{22}\left(\frac{\mathrm{d}x}{\mathrm{d}s}\right)^2 + A_{44}\left(\frac{\mathrm{d}y}{\mathrm{d}s}\right)^2 \right] \mathrm{d}s$$

$$a_{55}^p = \oint \left[K_{22}\left(\frac{\mathrm{d}y}{\mathrm{d}s}\right)^2 + A_{44}\left(\frac{\mathrm{d}x}{\mathrm{d}s}\right)^2 \right] \mathrm{d}s$$

$$a_{23}^p(z) = 0, \qquad a_{45}^p(z) = 0$$

The mass terms are

$$\begin{aligned}
b_4(z) &= M^2 b_4^p(z) + N^2 b_5^p(z) + 2MN b_6^p(z) \\
b_5(z) &= N^2 b_4^p(z) + M^2 b_5^p(z) - 2MN b_6^p(z) \\
b_{15}(z) &= M^2 b_{15}^p(z) + N^2 b_{14}^p(z) + 2MN b_{13}^p(z) \\
b_{14}(z) &= M^2 b_{14}^p(z) + N^2 b_{15}^p(z) - 2MN b_{13}^p(z) \\
b_6(z) &= MN\left[b_5^p(z) - b_4^p(z)\right] \\
b_{13}(z) &= MN\left[b_{14}^p(z) - b_{15}^p(z)\right] \\
b_1(z) &= b_1^p(z)
\end{aligned} \tag{A4}$$

where $M = \cos\beta(z)$ and $N = \sin\beta(z)$

In these expressions,

$$\left[b_1^p(z); b_4^p(z); b_5^p(z), b_6^p\right] = m_0 \oint [1; y^2; x^2; xy]\,\mathrm{d}s$$

$$= m_0\left\{2c(z) + 2c(z)S(z); c^3(z)S^2(z)[3 + S(z)]/6;\right.$$

$$\left. c^3(z)[1 + 3S(z)]/6; 0\right\}$$

$$\left[b_{13}^p(z); b_{14}^p(z); b_{15}^p(z)\right] = m_2 \oint \left[\frac{\mathrm{d}x}{\mathrm{d}s}\frac{\mathrm{d}y}{\mathrm{d}s}; \left(\frac{\mathrm{d}x}{\mathrm{d}s}\right)^2; \left(\frac{\mathrm{d}y}{\mathrm{d}s}\right)^2\right] \mathrm{d}s$$

$$= m_2[0; 2c(z); 2c(z)S(z)]$$

$$(m_0; m_2) = \int_{-h/2}^{h/2} [(\rho_c - \rho_m)V_m(1; n^2) + \rho_m(1; n^2)]\,\mathrm{d}n \tag{A5}$$

Acknowledgments

The authors extend their warmest thanks to the anonymous reviewers for their constructive comments that have contributed to the improvement of this paper.

References

[1]Aboudi, J., Pindera, M., and Arnold, S. M., "Thermoelastic Theory for the Response of Materials Functionally Graded in Two Directions," *International Journal of Solids and Structures*, Vol. 33, No. 7, 1996, pp. 931–966.

[2]Aboudi, J., Pindera, M. J., and Arnold, S. M., "Higher-Order Theory for Functionally Graded Materials," *Composites*, Part B, Vol. 30, 1999, pp. 777–832.

[3]Tanigawa, Y., "Theoretical Approach of Optimum Design for a Plate of Functionally Gradient Materials Under Thermal Loading," *Thermal Shock and Thermal Fatigue Behavior of Advanced Ceramics*, NATO Series E, Vol. 241, 1992, pp. 171–180.

[4]Noda, N., and Jin, Z. H., "Thermal Stress Intensity Factors for a Crack in a Strip of a Functionally Gradient Material," *International Journal of Solids and Structures*, Vol. 30, 1993, pp. 1039–1056.

[5]Birman, V., "Stability of Functionally Graded Hybrid Composite Plates," *Composites Engineering*, Vol. 5, 1995, pp. 913–921.

[6]Reddy, J. N., and Chin, C. D., "Thermomechanical Analysis of Functionally Graded Cylinders and Plates," *Journal of Thermal Stresses*, Vol. 21, 1998, pp. 593–626.

[7]Loy, C. T., Lam, K. Y., and Reddy, J. N., "Vibration of Functionally Graded Cylindrical Shells," *International Journal of Mechanical Sciences*, Vol. 41, No. 3, 1999, pp. 309–324.

[8]Praveen, G. N., and Reddy, J. N., "Nonlinear Transient Thermoelastic Analysis of Functionally Graded Ceramic–Metal Plates," *International Journal of Solids and Structures*, Vol. 35, No. 33, 1998, pp. 4457–4476.

[9]Gong, S. W., Lam, K. Y., and Reddy, J. N., "The Elastic Response of Functionally Graded Cylindrical Shells to Low-Velocity Impact," *International Journal of Impact Engineering*, Vol. 22, No. 4, 1999, pp. 397–417.

[10]Reddy, J. N., "Analysis of Functionally Graded Plates," *International Journal of Numerical Methods in Engineering*, No. 47, 2000, pp. 663–684.

[11]Pradhan, S. C., Loy, C. T., Lam, K. Y., and Reddy, J. N., "Vibration Characteristics of Functionally Graded Cylindrical Shells Under Various Boundary Conditions," *Journal of Applied Acoustics*, Vol. 61, No. 1, 2000, pp. 119–129.

[12]Cheng, Z.-W., and Batra, R. C., "Three-Dimensional Thermoelastic Deformation of a Functionally Graded Elliptic Plate," *Composites*, Part B, Vol. 31, No. 2, 2000, pp. 97–106.

[13]Yang, J., and Shen, H.-S., "Dynamic Response of Initially Stressed Functionally Graded Rectangular Thin Plates," *Journal of Composite Structures*, Vol. 54, 2001, pp. 497–508.

[14]Shen, H.-S., "Postbuckling Analysis of Axially-Loaded Functionally Graded Cylindrical Shells in Thermal Environments," *Composites Science and Technology*, Vol. 62, 2002, pp. 977–987.

[15]Sankar, B. V., and Tzeng, T. J., "Thermal Stresses in Functionally Graded Beams," *AIAA Journal*, Vol. 40, No. 6, 2002, pp. 1228–1232.

[16]Sankar, B. V., "An Elasticity Solution for Functionally Graded Beams," *Composites Science and Technology*, Vol. 61, 2001, pp. 689–696.

[17]Song, O., and Librescu, L., 'Structural Modeling and Free Vibration Analysis of Rotating Composite Thin-Walled Beams," *Journal of the American Helicopter Society*, Vol. 42, No. 4, 1997, pp. 358–369.

[18]Song, O., and Librescu, L., "Modeling and Dynamic Behavior of Rotating Blades Carrying a Tip Mass and Incorporating Adaptive Capabilities," *Acta Mechanica*, Vol. 134, 1999, pp. 169–197.

[19]Song, O., Librescu, L., and Oh, S.-Y., "Vibration of Pretwisted Adaptive Rotating Blades Modeled as Anisotropic Thin-Walled Beams," *AIAA Journal*, Vol. 39, No. 2, 2001, pp. 285–295.

[20]Song, O., Librescu, L., and Oh, S.-Y., "Dynamics of Pretwisted Rotating Thin-Walled Beams Operating in a Temperature Environment," *Journal of Thermal Stresses*, Vol. 24, No. 3, 2001, pp. 255–279.

[21]Song, O., Oh, S.-Y., and Librescu, L., "Dynamic Behavior of Elastically Tailored Rotating Blades Modeled as Pretwisted Thin-Walled Beams and Incorporating Adaptive Capabilities," *International Journal of Rotating Machinery*, Vol. 8, No. 1, 2002, pp. 13–25.

[22]Hodges, D. H., and Rutkowski, M. J., "Free-Vibration Analysis of Rotating Beams by a Variable-Order Finite Element," *AIAA Journal*, Vol. 19, No. 11, 1991, pp. 1459–1466.

[23]Lee, S. Y., and Lin, S. M., "Bending Vibrations of Rotating Nonuniform Timoshenko Beams with an Elastically Restrained Root," *Transactions of the American Society of Mechanical Engineers*, Paper 94-WA/ARM-8, 1994.

[24]Lee, S. Y., and Kuo, Y. H., "Bending Frequency of a Rotating Nonuniform Beam with an Elastically Restrained Root," *Journal of Sound and Vibration*, Vol. 154, No. 3, 1992, pp. 441–445.

[25]Palazotto, A. N., and Linnemann, P. E., "Vibration and Buckling Characteristics of Composite Cylindrical Panels Incorporating the Effects of a Higher Order Shear Theory," *International Journal of Solids and Structures*, Vol. 28, No. 3, 1991, pp. 341–361.

[26]Librescu, L., Meirovitch, L., and Na, S. S., "Control of Cantilevers Vibration via Structural Tailoring and Adaptive Materials," *AIAA Journal*, Vol. 35, No. 8, 1997, pp. 1309–1315.

B. V. Sankar
Associate Editor